Chemical Geology 674 (2025) 122588

Contents lists available at ScienceDirect

Chemical Geology

journal homepage: www.elsevier.com/locate/chemgeo

Desorption of rare earth elements (REEs) from schwertmannite under acid mine drainage (AMD) and AMD-seawater conditions

Joan Gutiérrez-León [a], Sergio Carrero [a,*], Devis Di Tommaso [b], Dimitrios Toroz [b], Alejandro Fernandez-Martinez [c], Antonio Aguilar [d], Alba Lozano [e,f], Rafael Pérez-López [g], Josep M. Soler [a], Jordi Cama [a]

[a] Institute of Environmental Assessment and Water Research (IDAEA), CSIC, 08034 Barcelona, Catalonia, Spain
[b] School of Physical and Chemical Sciences, Queen Mary University of London, Mile nd Road, London E1 4NS, UK
[c] Université Grenoble Alpes, Université Savoie Mont Blanc, CNRS, IRD, IFSTTAR, ISTerre, F-38000 Grenoble, France
[d] Institut de Chimie Moléculaire de Grenoble, UAR2607 CNRS, Université Grenoble Alpes, F-38000 Grenoble, France
[e] Department of Mine Technology, University of León, 24007 León, Spain
[f] Vice Rectorate of Research, University of Barcelona, 08011 Barcelona, Spain
[g] Department of Earth Sciences, University of Huelva, Campus 'El Carmen', 21071 Huelva, Spain

ARTICLE INFO

Editor: Karen Johannesson

Keywords:
Schwertmannite
Rare earth element
EXAFS
PDF
Desorption
AMD
Estuary

ABSTRACT

Schwertmannite as a sink for rare earth elements (REEs) in environments affected by acid mine drainage (AMD) plays a significant role in the fate of these elements. The conditions to precipitate schwertmannite (i.e., sulfate-rich water and pH between 2.5 and 3.5) are not suitable for this Fe-oxyhydroxysulfate ($Fe_8O_8(OH)_6SO_4$) to adsorb REEs. In estuaries where AMD-impacted rivers meet (e.g. the Odiel and the Tinto rivers in the Ría de Huelva estuary in SW Spain), AMD mixes with seawater raising the pH between 4.5 and 8, thereby enabling REE adsorption on schwertmannite at circumneutral pH. However, the estuarine tidal dynamics exposes REE-enriched schwertmannite to more acidic water, inducing REE desorption, which has yet to be studied.

In the present work, batch experiments were performed to study the REE desorption from a REE-enriched schwertmannite within the pH range 4.5–7 in the presence of sulfate at room temperature. Solution-chemistry data were used to obtain the REE desorption surface constants from different surface complexation. Desorption of a Lu-enriched schwertmannite at different pH was investigated with High Energy X-Ray Diffraction (HEXD) and Extended X-ray Adsorption Fine Structure (EXAFS) to characterize the changes in the surface complexes during desorption. The results indicate that (1) REEs desorb from schwertmannite at pH < 6 and desorption is pH dependent, (2) desorption of light REEs is higher than that of heavy REEs, (3) REE sorption onto schwertmannite surface is not a totally reversible reaction, and that (4) both monodentate and bidentate surface complexes are involved in the Lu-desorption reaction. These observations indicate that (1) REE-enriched schwertmannite remains stable in the areas of the estuary nearer the sea and that (2) tidal fluctuations displace schwertmannite colloids towards areas that are more affected by AMD, inducing REE desorption from schwertmannite.

1. Introduction

Although rare earth elements (REEs: lanthanides, yttrium and scandium) are scarce in the Earth's crust, their presence in surface water may have ecotoxicological impacts, such as reduction of plant growth, genotoxicity, neurotoxicity and bioaccumulation in fishes that could enter in the trophic chain (Chakhmouradian and Wall, 2012; Haque et al., 2014; Gwenzi et al., 2018). REEs can contaminate the environment because of disposal of solid waste in landfills, wastewater and atmospheric emission from electronical industrial processes (Tan et al., 2015; Işıldar et al., 2018), urban wastes (Lawrence et al., 2009; Klaver et al., 2014), fertilizers (He et al., 2010; Pagano et al., 2015) or mining activity (Ayora et al., 2016; Paulick and Machacek, 2017). From the different sources, mining activity is the most relevant in terms of intensity and extensity (Paulick and Machacek, 2017). Li et al. (2010) indicated that soils within a 7 km radius of a REE-processing plant were contaminated

* Corresponding author.
E-mail address: Sergio.carrero@idaea.csic.es (S. Carrero).

https://doi.org/10.1016/j.chemgeo.2024.122588
Received 8 October 2024; Received in revised form 18 December 2024; Accepted 18 December 2024
Available online 22 December 2024

with concentrations at least 100 times higher than the regional background. Likewise, Romero et al. (2010) observed that leaching from mining areas enriched in REEs could pollute surface water throughout hundreds of kilometres, being especially relevant in surface waters affected by acid mine drainage (AMDs; Ayora et al., 2016; Silva et al., 2022).

AMD from sulphide mineral weathering is highly acidic and rich in sulfate, Fe, Al and other metal(loid)s (e.g., Cu, Zn or As) (Moses et al., 1987; Bigham and Nordstrom, 2000; Nieto et al., 2013). Although initial sulphide ore deposits generally display low REE concentrations, AMDs concentrate REEs, reaching a ΣREE up to 1–11 mg L^{-1} (Ayora et al., 2022). These concentrations are several orders of magnitude higher than those in other water reservoirs such as ocean ($1.2{\cdot}10^{-6}$ mg L^{-1}), groundwater ($8.2{\cdot}10^{-6}$ mg L^{-1}), rivers ($1.1{\cdot}10^{-5}$ mg L^{-1}), or lakes ($2.6{\cdot}10^{-5}$ mg L^{-1}) (Merten et al., 2005; Ferreira da Silva et al., 2009; Noack et al., 2014; Ayora et al., 2016).

In Southwest Spain, AMDs from around 100 abandoned mines across the Iberian Pyritic Belt (IPB) release about 10.7, 2.1 and 5.5 tons of light REEs (LREEs), medium REEs (MREEs) and heavy REEs (HREEs), respectively (Sánchez-España et al., 2005; Nieto et al., 2013; León et al., 2021). Many of the AMD streams are tributaries along the two main rivers that drain the IPB (i.e., the Tinto and the Odiel rivers), in which the REE concentration is above 11 mg L^{-1}, and reach the sea through the Ría de Huelva estuary (Neira et al., 2022; Packman et al., 2023; Gutiérrez-León et al., 2024), affecting life and water quality.

Precipitation of schwertmannite ($Fe_8O_8(OH)_6SO_4{\cdot}nH_2O$; Bigham et al., 1994) controls the mobility of pollutants when AMD acidity is neutralized by mixing AMD with river or sea waters (Bigham and Nordstrom, 2019; Gutiérrez-León et al., 2024). Schwertmannite is a poorly-crystalline nanomineral with a tunnel-like structure formed by double chains of iron octahedra with sulfate tetrahedra located at inner and outer coordination spheres (Fernandez-Martinez et al., 2010; Wang et al., 2015, 2021; Sestu et al., 2017). It precipitates at a pH between 2.5 and 3.5 in the presence of sulfate and has a high surface area, which is positively charged at acidic pH (zero-charge point at pH 7; (Jönsson et al., 2005), making it a sink for aqueous oxyanions (e.g., arsenate, antimonate, chromate, phosphate, selenate and molybdate (Regenspurg and Peiffer, 2005; Manaka et al., 2007; Antelo et al., 2012; Li et al., 2016; Zhang et al., 2016; Carrero et al., 2017; Khamphila et al., 2017; Schoepfer et al., 2019; Schoepfer and Burton, 2021).

Under AMD conditions (pH < 3.5), aqueous REE species, mainly Ln (lanthanides, Y and Sc) sulfate complexes (i.e., $[LnSO4]^+$) are positively charged, resulting in mutual repulsion with schwertmannite surface. It is shown, however, that schwertmannite adsorbs Ln in the presence of sulfate at pH between 4.5 and 6.5 (Lozano et al., 2020). Since water of AMD-impacted estuaries (e.g. estuary of Ría de Huelva) has a pH between 3.5 and 8 and a high sulfate concentration (Gutiérrez-León et al., 2024), adsorption of $[LnSO4]^+$ onto schwertmannite colloids occur at pH > 4.5 (Elbaz-Poulichet and Dupuy, 1999; Lecomte et al., 2017). Carro et al. (2011) showed that the concentration of REEs (Σ[REE]) drops from 173 μg L^{-1} at pH 2.73 to 0.83 μg L^{-1} at pH 6.22 in the mixing zone of the Ría de Huelva estuary (SW Spain) in the presence of schwertmannite colloids. The non-conservative behaviour of REEs has been associated with surface adsorption onto schwertmannite colloids (Cánovas et al., 2021; Gutiérrez-León et al., 2024), which form when water of AMD-impacted rivers mixes with sea water (pH > 2.5). Colloids remain in suspension until water-mixing progresses and pH increases (pH > 4.5). At pH > 4.5, REE adsorption onto schwertmannite surface takes place, thus reducing the aqueous REE concentration (Elbaz-Poulichet and Dupuy, 1999; Gutiérrez-León et al., 2024). However, this overall process may be interfered by abrupt changes in pH during estuarine tidal cycles, in which schwertmannite colloids loaded with REEs are transported from seawater-influenced areas to more acidic areas in few hours (Cánovas et al., 2022; Packman et al., 2023; Pérez-López et al., 2023). Given that REE adsorption onto schwertmannite is pH dependent (Lozano et al., 2020), colloid displacement towards the more acidic pH areas may induce desorption of $LnSO_4$-surface complexes. The overall process results in a REE re-dissolution that increases availability of REEs in the estuary. But, REE desorption from schwertmannite has yet to be studied.

However, it should be highlighted that schwertmannite can transform into goethite over weeks or months (i.e., aging) depending on the pH and the sulphate and Fe(II) concentrations (Regenspurg and Peiffer, 2005; Acero et al., 2006; Burton et al., 2009; Paikaray et al., 2017; Paikaray, 2021). During the transformation, divalent cations and/or metalloids adsorbed onto schwertmannite are released back to solution (Acero et al., 2006). Gutiérrez-León et al. (2024) demonstrated the presence of schwertmannite at pH > 3.3 in the water of the AMD-impacted estuary of Ría de Huelva. Moreover, the phosphate released from an adjacent phosphogypsum stack enhances schwertmannite stability. Taking this into consideration, the aim of this paper is to better understand the REE-schwertmannite desorption under estuarine pH, although the occurrence of schwermannite aging cannot be ruled out. However, the study of the aging effect on the release of REEs during the schwertmannite-goethite transformation falls beyond the scope of this paper.

We seek to (1) elucidate the REE desorption on schwertmannite in the pH range between 4.5 and 7 in the presence of sulfate, (2) obtain the log *K* values of the REE desorption reactions, (3) characterize the molecular structure of the aqueous REE-sulfate species as well as the REE-schwertmannite surface complexes, and (4) model the desorption reactions. To this end, desorption batch experiments using a REE-rich schwertmannite (i.e., schwermannite enriched with LREEs, MREEs and HREEs) were performed under atmospheric conditions, pH 4.5–7 and $[SO_4^{2-}] = 2840$ mg L^{-1}. The log *K* values obtained for the desorption reactions were used to model the REE-retention at the pH range under study. High Energy X-Ray Diffraction (HEXD) with Pair Distribution Function (PDF) analyses, density functional theory (DFT) calculations and Extended X-ray Absorption Fine Structure (EXAFS) analyses were carried out to characterize the aqueous species and surface complexes. To this end, a synthetic schwertmannite only enriched in Lu (HREE) had to be used in order to avoid signal overlapping between rare earth elements. The results obtained are relevant for geochemical modeling and better understanding of REE behaviour under estuarine conditions.

2. Materials and methods

2.1. Schwertmannite characterization

Schwertmannite was synthesized following a standard procedure (Bigham et al., 1990), adding 10.8 g of $FeCl_3{\cdot}6H_2O$ and 3 g of Na_2SO_4 to 2 L of Milli-Q water. This solution was kept at 333 K for 12 min and, subsequently cooled to room temperature (298 ± 2 K). The solid was dialyzed (cellulose membrane: Spectra/Por® Dyalisis Membrane) in 15 L of Milli-Q water, which were renewed every 24 h until the specific conductance was <5 μS cm^{-1} for five consecutive days. After dialysis, the precipitate was centrifuged for 15 min at 4500 rpm (4150 RCF), frozen and lyophilized in an Alpha 2–4 LD plus freeze-dryer to avoid solid recrystallization. Powder X-ray diffraction (XRD) analysis of the synthesized samples was performed using a 2Θ goniometer Bruker D8 Advance diffractometer with Cu Kα radiation. The sample was scanned from 2 to 60 degrees 2Θ with a continuous scan at a rate of 0.025°/18 s. The specific surface area (m^2 g^{-1}) was obtained by the BET-N_2 sorption method using a Micrometrics Gemini V analyzer. The stoichiometry of the synthetic schwertmannite was calculated after digestion of 0.05 g in 5 mL of 65 % HNO_3 solution (Merck). The acidic solution was evaporated, and the obtained pellet was dissolved in 50 mL of Millipore Milli-Q water, acidified with 1 % HNO_3 solution, and stored in the refrigerator at 277 K for subsequent chemical analysis.

2.2. REE enrichment in schwertmannite

Schwertmannite was enriched with REEs following the method described by Lozano et al. (2020). A REE stock solution containing LREEs (La, Ce, Pr and Nd), MREEs (Sm, Eu, Gd, Tb and Dy), HREEs (Ho, Er, Tm, Yb, Lu and Y) and Sc was prepared by adding an ICP standard mix of 16 elements (excluding Pm) (Merck) and Na_2SO_4 salt in Milli-Q water. The final concentrations of each REE and SO_4^{2-} were 1 mg L^{-1} and 2840 mg L^{-1}, respectively. Although the concentrations of some REEs in the stock solution exceeded the concentrations in AMDs, this solution was prepared to have similar concentrations of the elements. The solution pH was adjusted to 6.5 (pH with the highest REE adsorption onto schwertmannite) by adding the desired volume of 0.05 M NH_4OH solution. Half a gram of schwertmannite was added to 0.5 L of stock solution (S/L ratio = 1 g L^{-1}). The resulting suspensions were shaken for 6 h and the pH was periodically re-adjusted to 6.5 by adding 0.05 M NH_4OH solution. Thereafter, the suspensions were centrifuged, the solid was washed several times with Milli-Q water and freeze-dried. The initial stock solution and the post-adsorption supernatants were filtered through 0.22 μm nylon membranes, acidified with 1 % HNO_3 solution, and kept at 277 K for subsequent chemical analysis.

A Lu enriched-schwertmannite was specifically prepared for synchrotron analyses to avoid signal overlapping between rare earth elements. REE interferences occur in EXAFS experiments in which the energy of L3-edge for different REEs is close to that of Lu L3-edge. Note that Lu was selected because the high atomic number and a lower desorption fraction yield more signal during the HEXD and EXAFS experiments. The stock Lu solution was made using an ICP Lu-standard solution (Merck) following the procedure described above. The final Lu and sulfate concentrations were 5 mg L^{-1} and 2840 mg L^{-1}, respectively. Although the Lu concentration in the stock solution was several orders of magnitude higher than that in AMD (Ayora et al., 2022), a high Lu loading (e.g., 5 ppm) on schwertmannite surface is necessary to analyse the bonding mechanisms using synchrotron radiation.

The concentration of adsorbed REEs by schwertmannite ($[REE]_{sch}$) was calculated using the following expression

$$[REE]_{sch} = [REE]_{initial} - [REE]_{final} \quad (1)$$

where $[REE]_{initial}$ and $[REE]_{final}$ are the concentrations of each REE in the stock and after-adsorption-experiment solutions (mg L^{-1}), respectively.

2.3. REE desorption from schwertmannite

To study the desorption kinetics (i.e., time to reach the equilibrium between REE enriched schwertmannite and desorption solution), a first series of batch experiments was performed at pH 4.85 for 2, 6, 12, 24 and 36 h with REE-enriched schwertmannite. A mass (0.01 g) of REE-enriched schwertmannite was suspended in 10 mL of 2840 mg L^{-1} SO_4^{2-} (by addition of Na_2SO_4 salt) solution with the desired pH, which was reached by addition of small volumes of 0.05 M NH_4OH solution.

To study the effect of pH on REE desorption, a second series of batch desorption experiments were performed with (i) 0.01 g of REE-enriched schwertmannite at pH 4.5, 4.75, 5.0, 5.25, 5.5, 5.75, 6.0, 6.25, 6.50, 6.75 and 7.0 and (ii) 0.01 g of a Lu-enriched schwertmannite at pH 4.5, 5.5 and 6.5. Desired pH was obtained as described above. Desorption experiments were run for 36 h. At this time, solution pH was stable for at least 12 h, ensuring equilibrium in accordance with desorption kinetics. All the experiments were run in duplicate, yielding a low standard deviation (SD < ± 5 %) that ensured the reproducibility of the results. The resulting suspensions from each experiment were centrifuged, and the supernatants were filtered through 0.22 μm nylon membranes, acidified and maintained in the refrigerator at 277 K for further chemical analysis. The remaining Lu-enriched schwertmannite was freeze-dried and stored for synchrotron analysis.

The desorbed REE fraction (%) was calculated according to this expression

$$\text{Desorbed REE fraction (\%)} = \left(1 - \frac{[REE]_{sch} - [REE]_{solution}}{[REE]_{sch}}\right) \bullet 100 \quad (2)$$

where $[REE]_{sch}$ and $[REE]_{solution}$ are the concentrations of each REE in the initial schwertmannite and in the final solution (mg L^{-1}), respectively. REE concentration on schwertmannite was calculated with Eq. (1).

2.4. REE desorption Model

A non-electrostatic model (NEM) was used to account for REE desorption on schwertmannite maintaining the hypothesis that is caused by an exchange between the $LnSO_4^+$ species (Ln = lanthanides, Y and Sc) and protons at n surface sites ($(XO)_n$) expressed as.

$$LnSO_4^+ + nXOH \leftrightharpoons (XO)_nLnSO_4^{1-n} + nH^+ \; K_{Ln} \quad (3)$$

The equilibrium constant for desorption reaction (DK_{Ln}) is defined as

$$DK_{Ln} = \frac{\{(XO)_nLnSO_4^{1-n}\} \cdot a_{H^+}^n}{a_{LnSO_4^+} \cdot \{XOH\}^n} \quad (4)$$

where a_{LnSO4+} and a_{H+} are the activities for REE aqueous complex and proton, respectively, $\{(XO)_nLnSO_4^{1-n}\}$ is the molar fraction of sorbed species ($\{(XO)_nLnSO_4^{1-n}\} = [(XO)_nLnSO_4^{1-n}]/T_{XOH}$), and $\{XOH\}$ is the molar fraction of free surface sites ($\{XOH\} = [XOH]/T_{XOH}$). Table 1 lists the DK_{Ln} values for the reactions.

The concentration of free surface sites $[XOH]$ is calculated as the difference between the total site concentration (T_{XOH}) and the sum of each occupied site

$$[XOH] = T_{XOH} - \sum n[(XO)_nLnSO_4^{1-n}] \quad (5)$$

Applying logarithms in Eq. (4) and rearranging, the following expression is obtained:

$$log\frac{[(XO)_nLnSO_4^{1-n}]}{a_{LnSO_4^+}} - nlog[XOH] + (n-1)logT_{XOH} = npH + logDK_{Ln} \quad (6)$$

in which the slope of the regression line is the number of occupied sites (n) in the reaction. Values of n close to 1 or 2 for the desorption experiment indicate the reaction of complexes in monodentate or bidentate coordination, respectively.

Table 1
Desorption constants ($Log\ DK_{Ln}$) values and their respective errors for bidentate and monodentate complexes. Calculations were made assuming $n = 2$ and $n = 1$ for bidentate and monodentate complexes, respectively.

Element	bidentate complex	log DK	error (± %)	monodentate complex	log DK	error (± %)
Sc	$(XO)_2ScSO_4^-$	−4.92	1.88	–	–	–
Y	$(XO)_2YSO_4^-$	−7.62	1.63	$XOYSO_4$	−1.92	3.70
La	$(XO)_2LaSO_4^-$	−7.98	2	$XOLaSO_4$	−2.28	2.18
Ce	$(XO)_2CeSO_4^-$	−7.77	1.76	$XOCeSO_4$	−2.00	3.98
Pr	$(XO)_2PrSO_4^-$	−7.60	1.73	$XOPrSO_4$	−1.90	3.67
Nd	$(XO)_2NdSO_4^-$	−7.49	1.91	$XONdSO_4$	−1.79	3.32
Sm	$(XO)_2SmSO_4^-$	−7.39	1.61	$XOSmSO_4$	−1.69	4.33
Eu	$(XO)_2EuSO_4^-$	−7.37	1.41	$XOEuSO_4$	−1.68	4.92
Gd	$(XO)_2GdSO_4^-$	−7.47	1.58	$XOGdSO_4$	−1.77	4.16
Tb	$(XO)_2TbSO_4^-$	−7.34	1.68	$XOTbSO_4$	−1.62	6.29
Dy	$(XO)_2DySO_4^-$	−7.37	1.13	$XODySO_4$	−1.64	6.51
Ho	$(XO)_2HoSO_4^-$	−7.36	1.22	$XOHoSO_4$	−1.64	7.15
Er	$(XO)_2ErSO_4^-$	−7.31	0.95	$XOErSO_4$	−1.59	7.87
Tm	$(XO)_2TmSO_4^-$	−7.21	1.18	$XOTmSO_4$	−1.63	7.65
Yb	$(XO)_2YbSO_4^-$	−7.08	0.86	$XOYbSO_4$	−1.58	10
Lu	$(XO)_2LuSO_4^-$	−7.06	1.06	$XOLuSO_4$	−1.62	9.44

2.5. Analytical techniques

A Crison® glass electrode calibrated with standard buffer solutions at pH 1.68, 4 and 7 was used to measure the pH in solution with an accuracy of 0.02 pH units. Inductively coupled plasma optical emission spectroscopy (ICP-OES) was employed to measure the concentrations of the major elements (S and Fe) with a Perkin-Elmer® Optima 3200 RL apparatus. The detection limits were 0.1 mg L^{-1} for S and 0.02 mg L^{-1} for Fe. The REE concentrations (Sc, Y, La, Ce, Pr, Nd, Sm, Eu, Gd, Tb, Dy, Ho, Er, Tm, Yb and Lu) in all solutions were determined by inductively coupled plasma mass spectrometry (ICP-MS) using a Perkin-Elmer®-SciexElan 6000 analyzer. The detection limits were 0.2 μg L^{-1} for REEs. The analytical error was calculated using standard solutions prepared from the Periodic Table Mix 3 for ICP TraceCERT™ solution (certified reference material (CRM); Sigma Aldrich) for REEs and from ICP multi-element standard solution (Merck) for S and Fe. Internal standard solutions were intercalated between samples to check the analytical accuracy, and the deviation from the stipulated values was always lower than 5 %.

A HEXD experiment was carried out at the beamline ID22 of the European Synchrotron Radiation Facility (ESRF) with solid samples retrieved from the Lu-enriched schwertmannite desorption experiments and with synthetic aqueous solutions with $LuSO_4^+$ species. The beamline provided a monochromatic X-ray beam with an energy of 70 KeV (λ = 0.1771 Å) for Lu-enriched schwertmannite samples and 61.86 KeV (λ = 0.2004 Å) for the $LuSO_4^+$ aqueous solutions. Both beams were calibrated with a CeO_2 standard (NIST 679b). Samples were loaded in polyamide (Kapton) capillaries. The diffraction patterns were collected employing a Perkin detector that was corrected and integrated using pyFAI (Kieffer and Karkoulis, 2013). PDFs were obtained by Fourier transformation of the structural factor, S(Q) (Qmax = 22.01 $Å^{-1}$), with the background scattering corrected (air and Kapton capillary scattering for Lu-enriched schwertmannite and additional Milli-Q water scattering in $LuSO_4^+$ aqueous solutions) with a PDFGetX3 software (Juhás et al., 2013). Differential pair distribution functions (d-PDF) were obtained by subtracting a reference PDF of the starting material (synthetic Lu-rich schwertmannite) from the PDFs of the samples after desorption at the different pHs.

The structural analysis of the Lu-enriched schwertmannite samples was performed at the CRG-FAME beamline (BM30)* in the ESRF. The ring was operated at 6 GeV with a nominal current of 200 mA in 7/8 + 1 mode. The beamline is equipped with a liquid-nitrogen-cooled doubled crystal Si(220) monochromator surrounded by two Rh-coated mirrors for harmonic rejection. The beam size on the sample was 200 × 100 μm (HxV, FWHM). The solid samples were arranged as 5 mm diameter pellets and covered with polyamide (Kapton)-type adhesive on sample holders. Standard of Lu_2O_3 was included for energy calibration in Lu L3-level. The experiment was carried out at 12 K using a helium cryostat to reduce the thermal vibration. Lutetieum L3-edge spectra were collected in fluorescence mode using a CANBERRA 13-elements Ge solid-state detector. The EXAFS data were scanned in a range between 9.1 and 9.88 keV for Lu L3-edge. EXAFS data reduction was performed using the Athena and Artemis software from IFFEFIT package (Ravel and Newville, 2005) by fit shell-by-shell, implementing three different hypothetical structural coordinations: i) bidentate binuclear inner sphere coordination "Lu shares two oxygens with two different Fe octahedrons"; ii) monodentate mononuclear inner sphere coordination "Lu shares one oxygen with one Fe octahedron"; and iii) monodentate binuclear inner sphere coordination "Lu shares one oxygen with two different Fe octahedrons". Backscattering phases and amplitude functions of the scattering paths were estimated using the Artemis software (Ravel and Newville, 2005). Several surface complexes between schwertmannite and $LuSO_4^+$ aqueous species were tested. The K weighted EXAFS spectra were fitted in the 2.2–8.4 $Å^{-1}$ range. The interatomic distance (R), Debye-Waller factor (σ^2) and Fermi energy levels (ΔE_0) were fitted using a least-squares refinement algorithm, whereas the coordination number (N) was fixed according to the DFT simulations. Statistical F tests were applied to determine the statistical significance of the difference EXAFS structural models. Details of F test analysis are described in section S1 of the Supporting Information.

2.6. DFT molecular calculation

Given that the lutetium molecular structure is necessary to build surface complexes in the EXAFS models, a computational quantum mechanical model of DFT was employed to determine the electron structure and the morphology of $LuSO_4^+$ molecules using the spatial dependent electron density. Calculations of the metal complexes were optimized with the Gaussian16 package (Frisch et al., 2016). The B3LYP exchange-correlation functional (Becke, 1993; Stephen et al., 1994) was used together with the def2-TZVP ECP basis set (Weigend and Ahlrichs, 2005) for the atoms of metals, Lu and sulphur. The oxygen and hydrogen atoms were treated with the LANL2DZ basis set (Hay and Wadt, 1985; Wadt and Hay, 1985). The B3LYP level of theory has been widely used to study the reactions of transition metal complexes (Jemmis et al., 2000; Ezzat et al., 2020). Calculations were performed without symmetry and geometry constraints in both the gas phase and continuum solvation model. The continuum solvation model used to describe the aqueous environment was the conductor-like polarizable continuum model (CPCM) (Cossi et al., 2003). In all the calculations, water molecules coordinated with the lanthanide metal centre were treated explicitly, and the implicit continuum model described solvation around the nine-coordinated lanthanide complex. Calculations were performed with molecular models of $[Lu(H_2O)]^{3+}$ on the basis of a tricapped trigonal prism. A microsolvation-continuum description of the sulfate ion ($SO_4(H_2O)_n$ with n = 1–10) was employed to obtain an accurate evaluation of the solvation-free energy of doubly charged anion SO_4^{2-} (Pliego and Riveros, 2020).

2.7. REE speciation

Aqueous REE speciation was calculated using the PHREEQC code (Parkhurst and Appelo, 1999) and the Donee Thermoddem_V1.10 database (Blanc et al., 2012). The values of the equilibrium constants at zero ionic strength and 298 K for aqueous speciation of lanthanides, Y and Sc (Ln, Lozano et al., 2019) and the equilibrium constants for Sc $(OH)^{2+}$, $Sc(OH)_2^+$ and $Sc(OH)_3$ (Wood and Samson, 2006), $LnF^{2+}$and LnF_2^+ (Luo and Millero, 2004) and $LnCl^{2+}$,$LnSO_4^+$, (Luo and Byrne, 2001; Schijf and Byrne, 2004) $Ln(OH)^{2+}$ (Klungness and Byrne, 2000), $Ln(OH)_2^+$, $Ln(OH)_3^0$ (Lee and Byrne, 1992) $Ln(CO)_3^+$, $LnHCO_3^{2+}$, $Ln(CO_3)_2^-$ (Luo and Byrne, 2004) and $Ln(NO)_3^{2+}$ (Millero, 1992) were added to the database. Moreover, solubility constants for the solid REE phases (Ln $(OH)_3$ and $Ln(OH)_3$(am)) were added from the Lawrence Livermore National Lab (LLNL) database (Spahiu and Bruno, 1995; Johnson et al., 2000). The equilibrium constants for aqueous inorganic speciation are listed in Table S1.

3. Results

3.1. Schwertmannite characterization

Schwertmannite is a nanocrystalline phase that forms aggregated particles (diameter ≈ 1–5 μm) and displays a "pin-cushion" morphology (Bigham et al., 1996; Bigham and Nordstrom, 2000). Digestion of the synthetic solid yielded a chemical composition of 7.91 mol_{Fe} mol_{Sch}^{-1}, which nears the ideal schwertmannite values (8 mol_{Fe} mol_{Sch}^{-1}), and 0.98 mol_S mol_{Sch}^{-1} (ideal stoichiometry is 1 mol_S mol_{Sch}^{-1}). This results in a stoichiometry composition of $Fe_8O_8(OH)_{5.96}(SO_4)_{1.02}$ (Table S2). Powder XRD patterns of the synthesized solid were affected by Fe fluorescence, preventing from obtaining any signal. However, the XRD pattern of the REE-enriched schwertmannite showed a characteristic, broad

peak at 35° 2θ related to (221) reflexion (Fig. S1) (Bigham et al., 1996). Moreover, HEXD patterns of synthetic schwertmannite, before and after REE adsorption/desorption experiments, were similar to those reported for schwertmannite using the same technique (Fig. S1) (Fernandez-Martinez et al., 2010). After adsorption experiments, the REE concentration ranged between 0.0052 and 0.0064 mol mol_{Sch}^{-1} for lanthanides, 0.022 mol mol_{Sch}^{-1} for Sc and 0.0105 mol mol_{Sch}^{-1} for Y in the REE-rich schwertmannite, whereas the Lu-rich schwertmannite contained 0.034 mol_{Lu} mol_{Sch}^{-1}. Therefore, adsorption removed more that 98 % of REEs from solution, providing evidence that the selected conditions were optimal to prepare REE-enriched schwertmannite. Stoichiometry values after digestions are given in Table S3.

The concentration of the schwertmannite surface sites was calculated using the site density of 4.75 sites nm^{-2}, which takes into account the number of single coordinated sites on the faces of the unit cell (Fernandez-Martinez et al., 2010). The concentration of occupied sites by REE ($\sum [(XO)_n LnSO_4^{1-n}]$) after REE enrichment of pure schwertmannite accounted for less than 0.5 % of total sites. The measured specific surface area for the synthetic schwertmannite (157 $m^2\ g^{-1}$) was in the same order of magnitude to previously reported values (175–200 $m^2\ g^{-1}$, Regenspurg et al., 2004, Antelo et al., 2012, Lozano et al., 2020). Thus, the calculated total site concentration was 1240 μmol g^{-1}.

3.2. REE desorption

REE concentrations measured in the pre- and post-desorption solutions corroborated that REE-enriched schwertmannite releases the REEs to the solution (Table S3). The kinetic desorption experiments showed a sharp increase of most of the REEs in solution up to 6 h. Thereafter, a gradual desorption occurred until the system reached equilibrium after 24 h (Fig. S2). As regards Sc, a slight desorption commenced after 12 h, reaching steady state at about 24 h. Fig. 1 shows that REE desorption occurred at pH ≤ 6.75, 6.5 and 6.25 for LREEs, MREEs and HREEs, respectively. The desorbed fraction (%) gradually increased with a decrease in pH, reaching values between 86 % and 73 % from La to Lu, respectively, at pH ≈ 4.5. Sc displayed a lower desorption pH, starting at pH < 5.5 and reaching a desorbed fraction of 45 % at pH 4.5.

3.3. Structure of the Lu aqueous complex

Fig. 2 shows the PDF analysis of the $LuSO_4^+$ aqueous solution. Note that the background intensity from air, Kapton capillary and Milli-Q water scattering was subtracted. The PDF showed peaks at 1.45 Å and 2.33 Å correlated with the S—O interatomic distance inside the sulfate tetrahedra and the Lu—O interatomic distance of the first coordination shell, respectively. Moreover, a peak at ≈ 3.46 Å was associated with the Lu—S distance. The DFT calculations yielded a Lu—O coordination number (*N*) of 8 and a single share oxygen with the sulfate tetrahedron. Similar *N* in the Lu—O coordination was previously reported for other Lu species as Lu^{3+}- and $LuCl^{2+}$ (Kowall et al., 1995; Yaita et al., 1999; Allen et al., 2000). DFT calculations suggest that Lu—O distances are

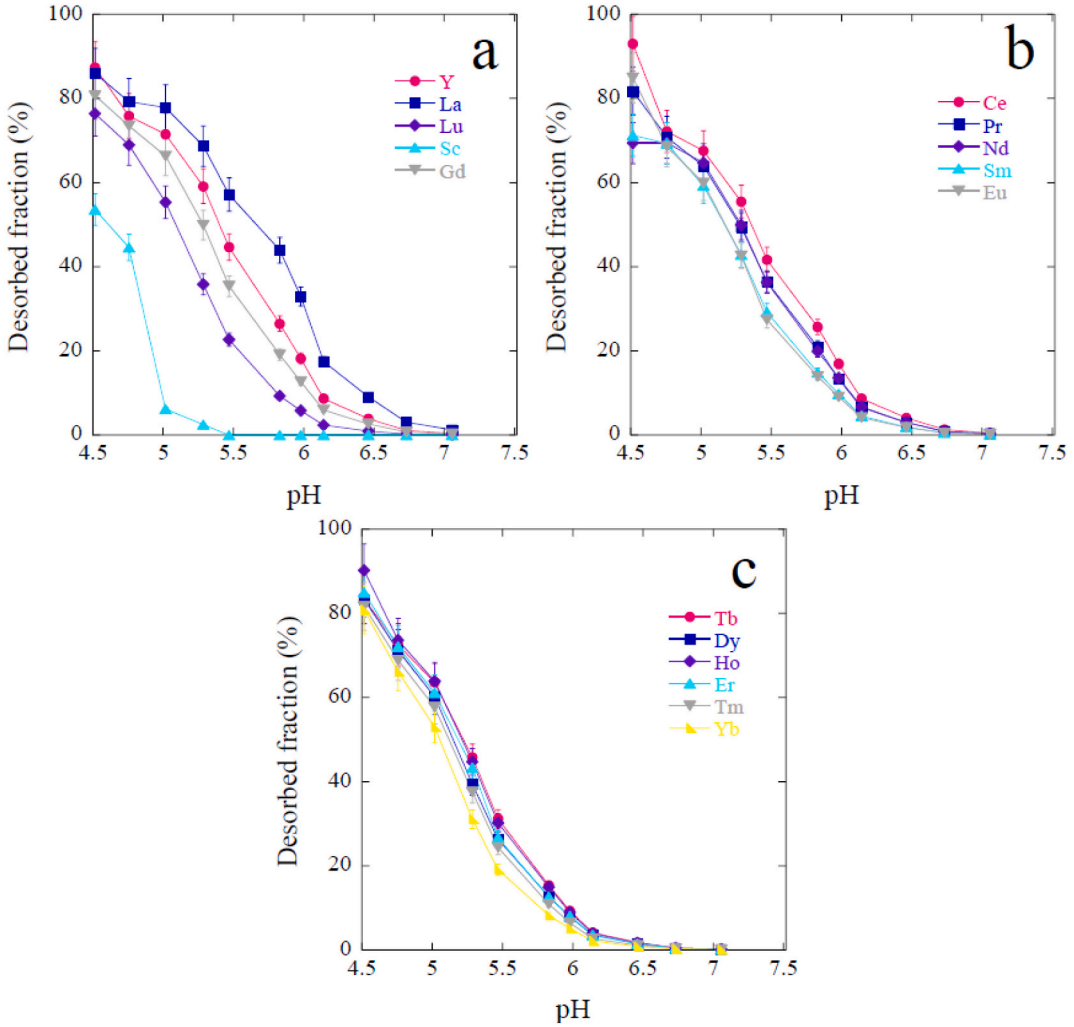

Fig. 1. Desorbed REE fraction in solution with 2840 mg L^{-1} of sulfate from synthetic schwertmannite. Error bars range between 1 % and 7 %.

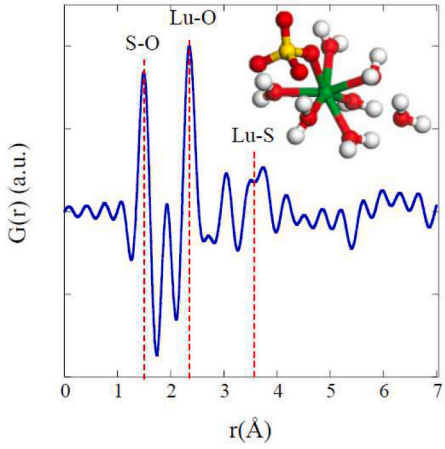

Fig. 2. PDF analysis of the $LuSO_4^+$ aqueous solution after being subtracted the background intensity from air and the Milli-Q water signal. PDF is normalized with the Lu—O peak. Dashed lines indicate interatomic distances of S—O, Lu—O and Lu—S bonds at 1.45 Å, 2.33 Å and 3.46 Å, respectively. The molecule geometry is calculated by CPCM; red, yellow, green and white balls indicate O, S, Lu and H atoms, respectively. (For interpretation of the references to colour in this figure legend, the reader is referred to the web version of this article.)

within the 2.30–2.33 Å range with the exception of two oxygens that are located at ≈ 2.20 Å. Therefore, identified Lu—O distance in the $LuSO_4^+$ molecule was similar to values reported for free Lu^{3+} ion and its coordinated water molecules (i.e., 2.31(2) Å) (Persson et al., 2008; Finck et al., 2019).

4. Discussion

4.1. REE affinity with the schwertmannite surface

As mentioned in the introduction, schwertmannite aging depends on the pH and the sulphate and Fe(II) concentration. This process leads to a decrease in the adsorption capacity and to a consequent instability of sorbed elements (Regenspurg and Peiffer, 2005; Acero et al., 2006; Burton et al., 2009; Paikaray et al., 2017; Paikaray, 2021). However, XRD and HEXD patterns of the schwertmannite samples before and after the REE desorption experiments showed only peaks of schwertmannite (Fig. S1). In the experiments, schwertmannite was suspended in water up to 36 h, a time span that is much shorter than the time required for the aging process. Hence, schwertmannite aging did not occur in the batch experiments, and the REE release was only caused by REE desorption. Moreover, PhreeqC-calculated saturation indexes (SI) of the final solutions (Fig. S3) indicate that the solutions were undersaturated with respect to REE-hydroxides and supersaturated with respect to schwertmannite. Therefore, schwertmannite dissolution followed by precipitation of secondary Fe- and/or REE-phases are improbable to occur during desorption reactions.

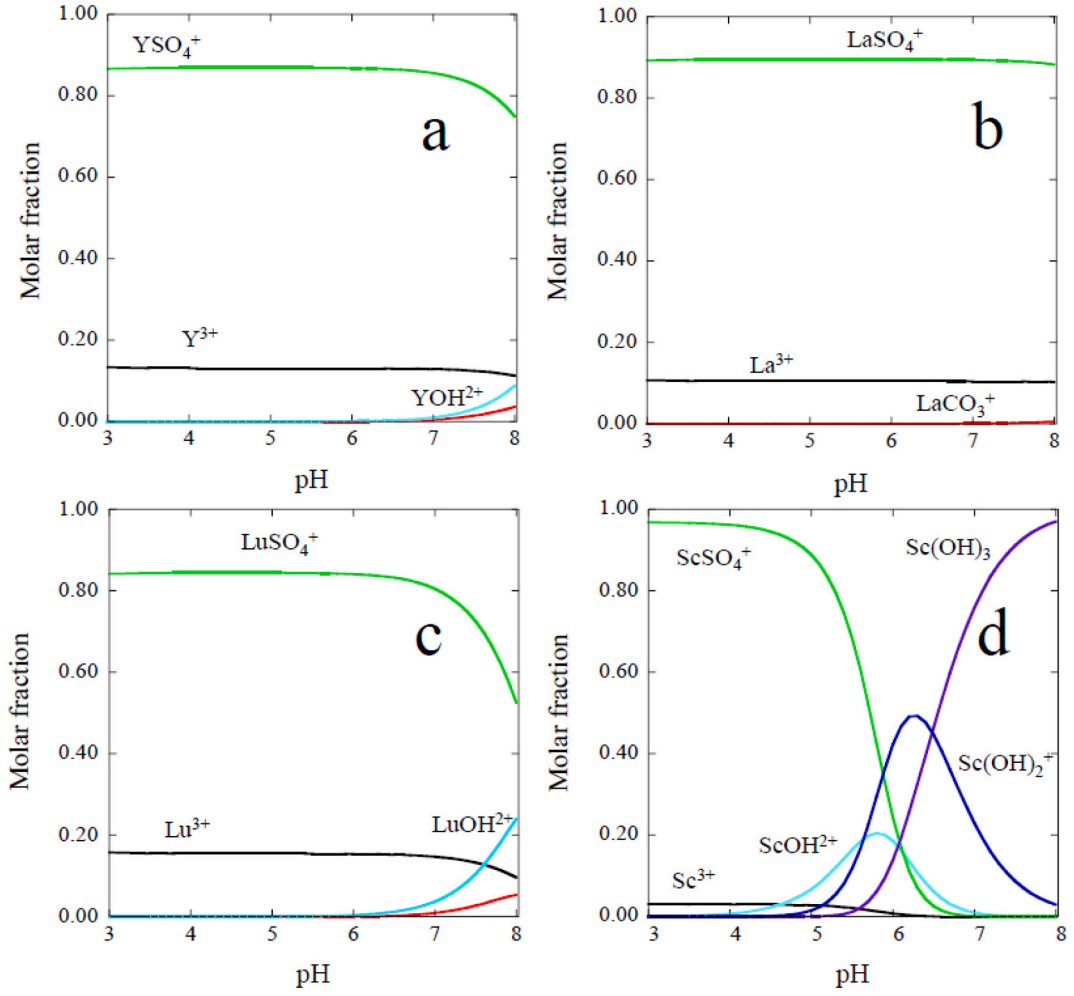

Fig. 3. Aqueous speciation with pH of (a) Y, (b) Sc, (c) La and (d) Lu in a 2840 mg L^{-1} sulfate solution at 298 K and atmospheric pCO_2.

REE aqueous speciation under experimental desorption conditions (i.e., pH range of 3–8, 1 mg L^{-1} of each REE and 2840 mg L^{-1} of SO_4^{-2}) shows that (1) the positively-charged aqueous $LnSO_4^+$ complexes predominate (87 % for $LaSO_4^+$ and 82 % of $LuSO_4^+$), (2) the free Ln^{3+}-ion species range between 12 % (La^{3+}) and 18 % (Lu^{3+}) and that (3) the $LnCO_3^+$ complexes only form for HREEs at a pH higher than the experimental conditions (5 % for YCO_3^+ and 10 % for $LuCO_3^+$) (Fig. 3 and S4). Therefore, stable REE aqueous and surface speciation coincides (except for Sc at pH > 5.5, $ScSO_4^+$ is <50 %) during desorption. Considering that the $LnSO_4^+$ species has been described as the main candidate to interact with schwertmannite surface (Lozano et al., 2020), the interference of the low proportion of secondary REE species (i.e., Ln^{3+} and $LnCO_3^+$) and/or adsorbed $LnSO_4^+$ transformation into Ln^{3+} and $LnOH^+$ is ruled out in the desorption experiment.

Batch experiments showed that REE desorption from schwertmannite is pH dependent (Fig. 1). Desorption is most effective at the lowest pH (4.85), releasing 60–80 % of sorbed REEs on the surface. Therefore, an increase in positive charge at pH < 7 reduces the affinity of schwertmannite surface with cations and the stability of the $LnSO_4^+$ species. Although schwertmannite affinity for cations is strong at pH > 7 (Jönsson et al., 2005; Antelo et al., 2012), adsorption of divalent cations onto schwertmannite surface (e.g., Cu and Pb) has been observed at a pH lower than the zero-charge pH (i.e., 6.6–7) (Webster et al., 1998; Shi et al., 2021). Furthermore, the amount of REEs that remains on schwertmannite surface after desorption at pH 4.5–6.5 is between 10 % and 15 % higher than the reported schwertmannite adsorption capacity under similar conditions (Lozano et al., 2020). This indicates that $LnSO_4^+$ sorption onto schwertmannite is not a totally reversible reaction. As a result, a fifth of previously sorbed REEs do not desorb even when schwertmannite equilibrates with solutions, which have physicochemical conditions that differ from optimum values for REE adsorption (i.e., pH = 6.5).

In contrast, Sc behaves differently (Fig. 1a). Desorption starts at a pH 5.5., i.e., one pH unit lower than that of the other $LnSO_4^+$ species (pH = 6.5), as $ScSO_4^+$ predominates (Fig. 3b). This indicates that previously adsorbed $ScSO_4^+$ is not suitable for desorption until this species is stable in solution (Zhang and Honaker, 2018). In addition, Sc is the REE with a lower desorption fraction than the rest of REEs (i.e., 50 % vs 80 % in HREEs). The higher surface affinity for Sc is probably due to its lower ionic radius, allowing $ScSO_4^+$ molecules to accommodate on the surface structure with low deformation during adsorption reaction. This enables the formation of stronger covalent bonds onto the mineral surface as reported for goethite, in which Sc forms bidentate binuclear binding inner sphere complexes (Qin et al., 2021).

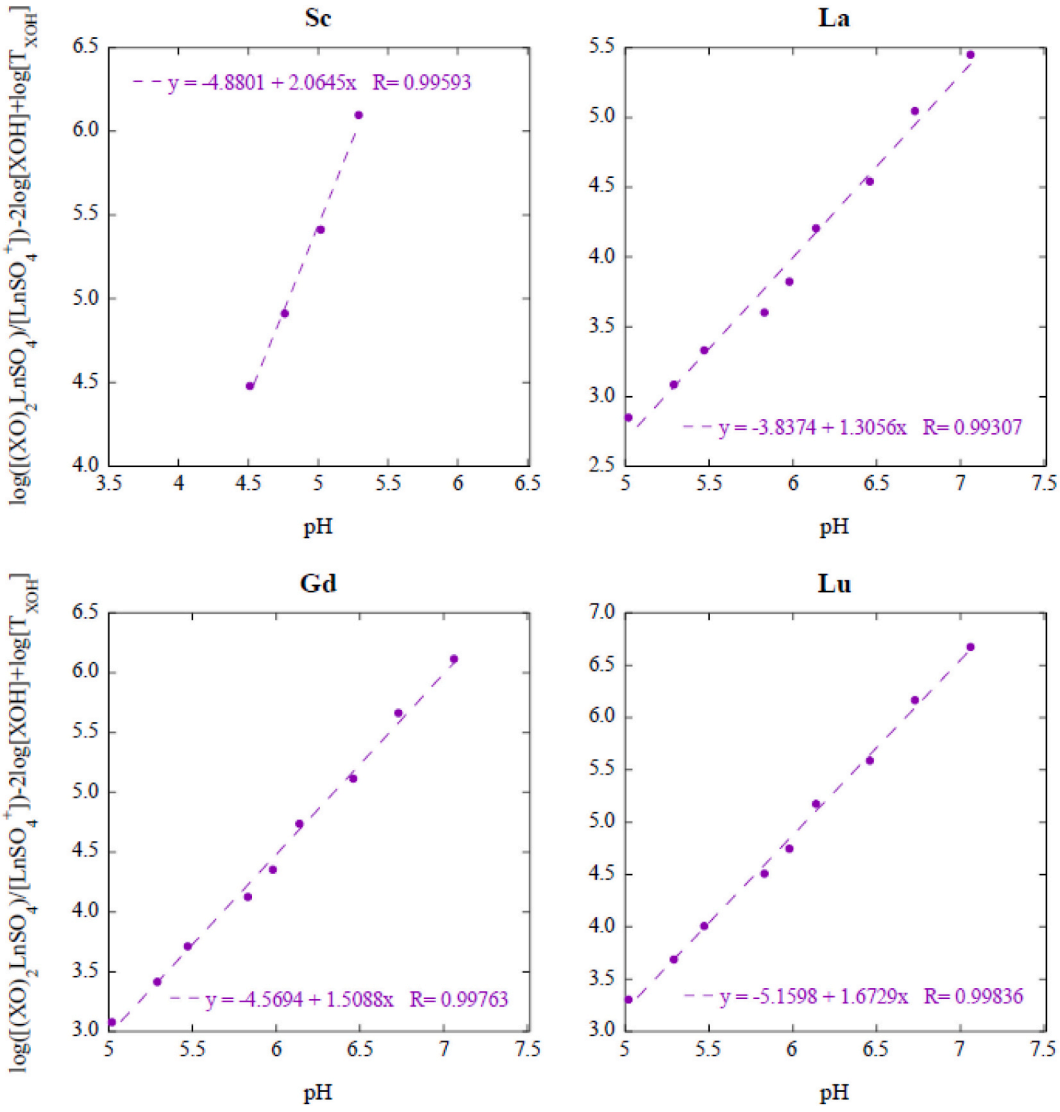

Fig. 4. Linear regressions for Sc, La, Gd and Lu experimental data using Eq. (8). Note that the slope values for lanthanides range between 1.3 and 1.67 whereas the slope is 2 for Sc.

4.2. Desorption model

4.2.1. Desorption equilibrium constants

Desorption experiments show that REE sorption onto schwertmannite surface is not totally reversible, indicating that equilibrium constants for REE desorption are necessary to model the behaviour of REEs in natural systems. The use of Eq. (6) and the desorption results yields linear correlations with n that varies between 1.3 (LREEs) and 1.7 (HREEs) and $n = 2$ for Sc (Figs. 4 and S5). These values are close to those of adsorption models (Lozano et al., 2020), in which lanthanides and Y adsorb through monodentate and bidentate surface binding, and Sc does it through bidentate surface binding. Therefore, the desorption equilibrium constants (log DK_{Ln}) for lanthanides and Y were obtained considering desorption from both monodentate (slope and occupied sites (n) = 1) and bidentate (slope and occupied sites (n) = 2) surface complexes. Only bidentate complexes were considered for Sc (Table 1). The desorption equilibrium constants are higher than those for adsorption (AK_{Ln}) reported by Lozano et al. (2020) who only considered bidentate coordination. The differences between log AK_{Ln} and log DK_{Ln} are +4, +3 and + 2 for LREEs, MREEs and HREEs, respectively. This corroborates that REE sorption is not a totally reversible reaction and that HREEs desorbed less than LREEs (log $DK_{La} = -3.84$ vs log $AK_{Lu} = -5.16$; Fig. 4 and S4). In this study, the calculated DK_{Ln} values for desorption of both surface complexes have been implemented in the desorption model to estimate their contribution in REE-schwertmannite desorption.

4.2.2. Model validation

Using PhreeqC, the *log* DK_{Ln} values obtained were used to calculate the desorbed fraction at the experimental conditions ($T = 298$ K, $pCO_2 = 3.5$ bar and [sulfate] = 2840 mg·L^{-1}) in a two-step simulation. First, the schwertmannite surface was equilibrated with a REE-rich solution at pH 6.5 in the presence of sulfate to enable the formation of monodentate and bidentate bindings. Thereafter, to simulate the desorption experiments, the surface was equilibrated with a REE-free solution with the same sulfate concentration and a pH ranging between 3.5 and 7.5. The model, in which equilibrium constants for desorption from monodentate and bidentate ligands were implemented, reproduces satisfactorily the experimental desorption edges (Figs. 5 and S6), demonstrating a combination of bidentate and monodentate surface complexes for REEs and Y. However, only bidentate surface complexes take place for Sc.

Lozano et al. (2020) suggested lanthanide adsorption on schwertmannite via bidentate surface. By contrast, desorption is represented by a combination of both monodentate and bidentate complexes in our study. This discrepancy could be attributed to the transformation of bidentate to monodentate surface complexes with subsequent desorption. Considering monodentate and bidentate models separately, REE desorption from bidentate accounts better at a higher pH (up to ≈ 6), whereas monodentate shows a greater influence on the desorbed fraction at pH < 6. Moreover, schwertmannite surface is more positively

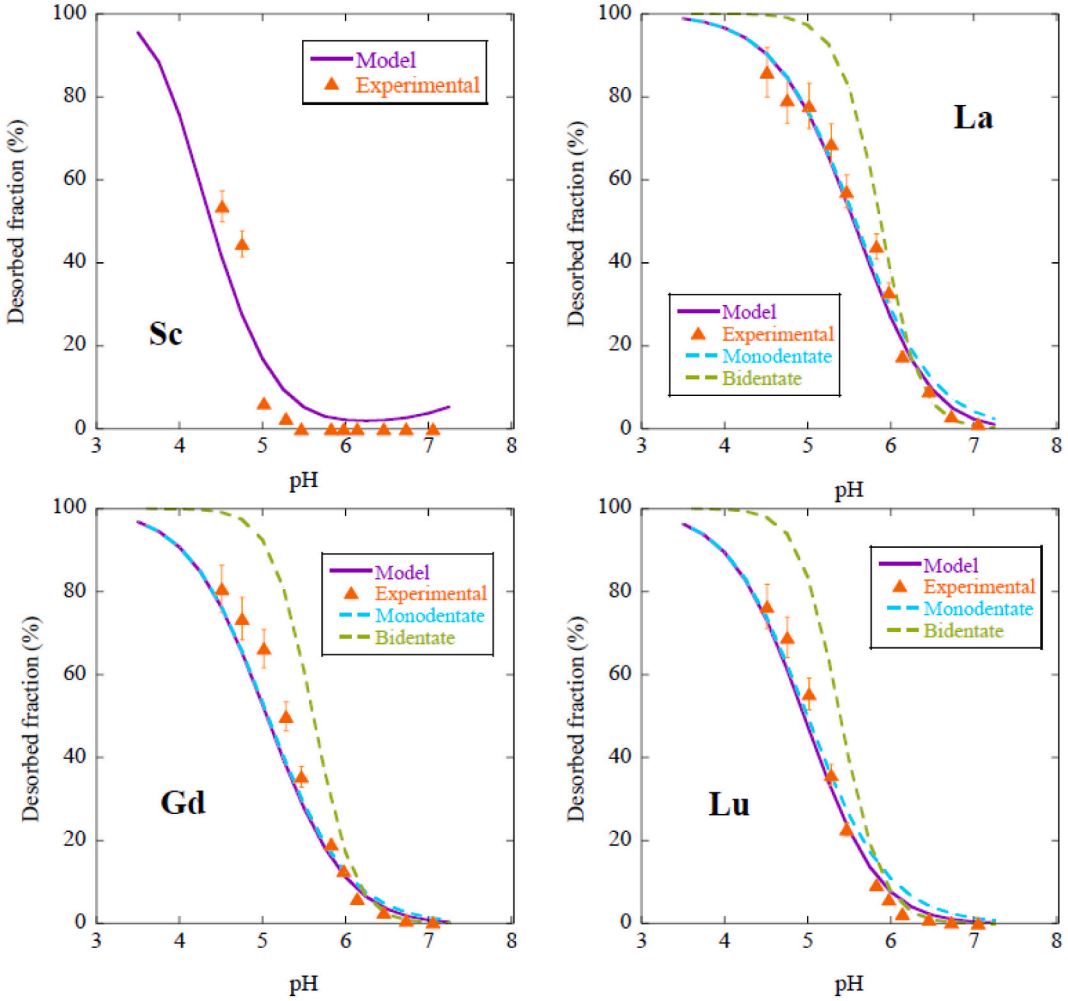

Fig. 5. Simulations of Sc, La, Gd and Lu desorption experiments using the complexation constants listed in Table 1. Models for only monodentate and bidentate are shown in blue and green dashed lines, respectively. (For interpretation of the references to colour in this figure legend, the reader is referred to the web version of this article.)

charged at low pH, reducing the number of available sites for cation adsorption (Webster et al., 1998; Swedlund and Webster, 2001). Therefore, the desorption models indicate that initial bidentate coordination (i.e., adsorption coordination) transforms into monodentate during desorption at pH < 6, reducing the REE stability on schwertmannite surface and enhancing the REE release to solution.

4.3. Atomistic model of the $LuSO_4^+$ surface complex

Lu bonding in schwertmannite surface (Fig. 6) after Lu adsorption (LuA) and after Lu desorption experiments at pH 6.5, 5.5 and 4.4 (Lu6.5, Lu5.5 and Lu4.5, respectively) was characterized using EXAFS and HEXD with d-PDF analysis (Figs. 7 and 8). Among REEs, Lu was selected for the synchrotron experiments because it hardly desorbs in comparison with the other lanthanides, providing more signal in the HEXD and EXAFS experiments. Owing to the decrease in the Lu signal in the desorption experiments run at a low pH, the k^3 range in the EXAFS spectra to implement the Fourier transform was set between 2.2 and 12.5 $Å^{-1}$. In this range, only the samples retrieved from the adsorption and desorption experiments at pH 6.5 (i.e., LuA and Lu6.5) showed a good signal-to-noise rate in K > 10 $Å^{-1}$. Since the samples of the desorption experiments run at pH < 6.5 displayed low Lu concentration for EXAFS analysis, the results obtained are inconclusive.

Three inner-sphere surface complexes (monodentate mononuclear, monodentate binuclear and bidentate binuclear; Fig. 6) were tested to model the coordination of the adsorbed $LuSO_4^+$ molecule. The geometry of the $LuSO_4^+$ molecule was obtained using DFT models, resulting in eight Lu—O first-shell paths (6 with $R = 2.33$ Å and 2 with $R = 2.20$ Å) and one Lu—S path ($R = 3.64$ Å). The bidentate binuclear surface complex shares two O atoms with two different octahedral Fe atoms (Fig. 6a), yielding a Lu—Fe path ($N = 2$ and $R = 4.53$ Å). The monodentate mononuclear surface complex shares one O with one octahedral Fe (Fig. 6b) leading to a single Lu—Fe path ($N = 1$ and $R = 4.56$ Å). In the monodentate binuclear surface complex, one O is shared with two octahedral Fe (Fig. 6c), accounting for two Lu—Fe paths ($N = 2$ and $R = 3.7$ Å). Note that paths with a negligible effect on the model (e.g. Lu-O-O) were not included.

Table 2 lists the parameters of the Lu-EXAFS models (LuA sample), and the fitting parameters for each sample are given in Tables S4–6. Overall, the distances for the Lu—O paths maintain their initial values ($R = 2.20$ Å and 2.33 Å), and the predicted Lu—S interatomic distance ranges between 3.58 Å and 3.62 Å in all the tested structural models. However, an N value of 2 is obtained for the Lu—S path in contrast to Lu aqueous speciation according to DFT models. It is thus deduced that the structural sulfate in the schwertmannite surface interacts with sorbed Lu, increasing $N_{Lu\text{-}S}$ as $LuSO_4^+$ was adsorbed.

The k range around 10.2 $Å^{-1}$ poses a limitation on determining the Lu—Fe distal paths. Hence, these paths in the models are taken as a complement to the chemical data of the batch desorption experiment and the d-PDF analysis, especially in samples Lu5.5 and Lu4.5. The Lu—Fe path distances in the bidentate binuclear and monodentate mononuclear models are similar (R ranges between 4.52 Å and 4.63 Å). Monodentate binuclear models show the highest χ^2 values suggesting a strong surface deformation to adjust $LuSO_4^+$ molecules (e.g., $R = 4.17$ Å with $\Delta r = -0.57$). These results indicate that monodentate binuclear coordination is geometrically invalid and should be ruled out. Figs. 7 and S7 show the experimental and fitted curves of the k^3-weighted EXAFS spectra and their Fourier transform amplitude for both the monodentate mononuclear and the bidentate binuclear coordination. The samples run at a higher pH (LuA and Lu6.5) yield satisfactory fittings, and the F-test calculations show a level of confident of ≈ 50 % in tested models (i.e., bidentate binuclear and monodentate mononuclear). This suggests that both models are alike and cannot be discarded at any pH (Table S7). However, EXAFS data and F-test analysis in Lu5.5 and Lu4.5 seem to indicate an increased role of monodentate ligands of the surface coordination in the non-desorbed portion of Lu after desorption at low pHs, which agrees with the desorption models (Fig. 5). Nevertheless, the low signal does not allow for a conclusive interpretation.

Similar results were observed in the d-PDF analysis, in which positive peaks at 2.33 Å, 3.6 Å and 4.55 Å could correlate with the Lu—O, Lu—S and Lu—Fe distances, respectively, in agreement with the EXAFS models for both bidentate binuclear and monodentate mononuclear coordination (Fig. 8 and Tables S4-S6). In addition, a higher Lu content implies the presence of more intense negative peaks at 3.4 and 5.45 Å, which correlate with the Fe—Fe distances inside the octahedral structural frame (Fernandez-Martinez et al., 2010; Wang et al., 2015, 2021) (Fig. 8). Therefore, $LuSO_4^+$ incorporation leads to a structural deformation where octahedral Fe must rotate to accommodate the adsorbed molecule. Considering Lu as the smallest element in the lanthanide series, adsorption of $LnSO_4^+$ having Ln a larger radius (i.e., element with lower atomic number), higher coordination number (i.e., 9) and longer interatomic Ln-O distances (e.g., La—O above 2.4 Å; Zhang et al., 2024)

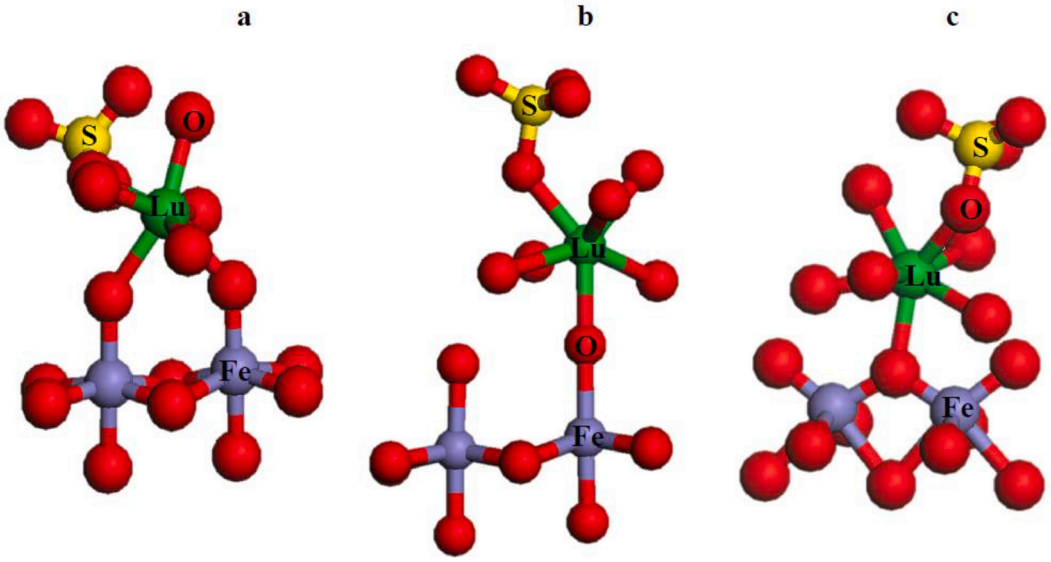

Fig. 6. Atomistic representations of the three models for $LuSO_4^+$ adsorption. The aqueous complex is attached to Fe octahedra by different coordinations. The inner sphere surface complexes considered in our study are: (a) bidentate binuclear, (b) monodentate mononuclear, and (c) monodentate binuclear.

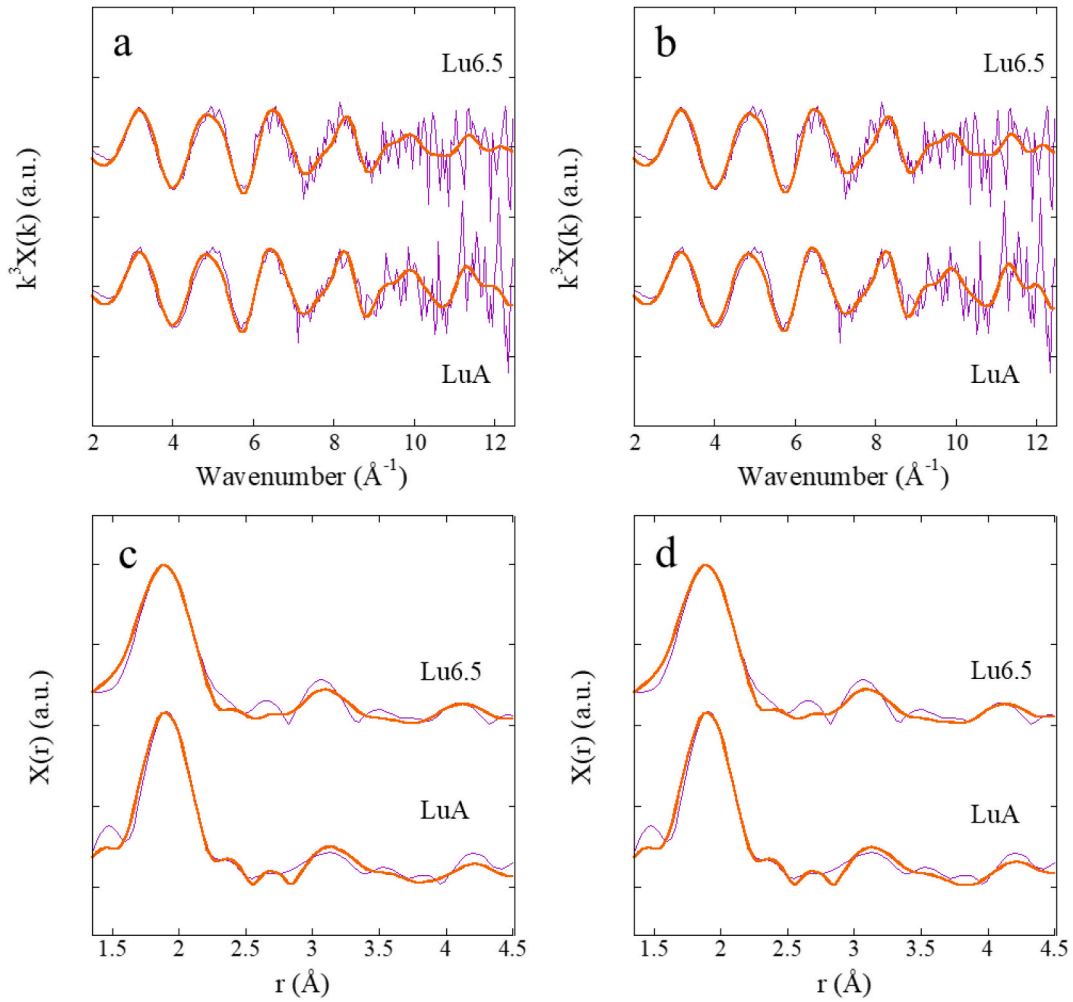

Fig. 7. K^3-weighted EXAFS spectra (a, b) at the Lu L3-edge and their respective Fourier transform (c, d). Data for LuA and Lu6.5 represent schwertmannite surface after Lu adsorption and after Lu desorption at pH 6.5, respectively. EXAFS have been fitted considering bidentate binuclear coordination (a, c) and monodentate mononuclear coordination (b, d). Experimental data is plotted as purple lines and fit data as orange lines. (For interpretation of the references to colour in this figure legend, the reader is referred to the web version of this article.)

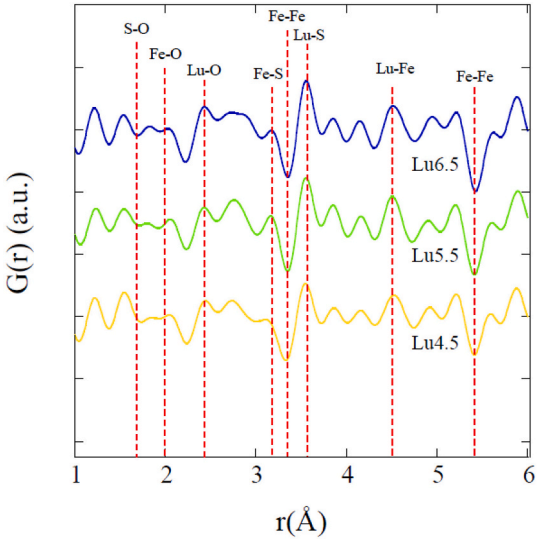

Fig. 8. d-PDF (pure schwertmannite-subtracted) of the Lu-rich schwertmannite after desorption at pH 6.5, 5.5 and 4.5. The position of main atomic-pairs in schwertmannite structure (Fernandez-Martinez et al., 2010) and $LuSO_4^+$ is indicated by vertical dashed lines.

leads to a higher structural distortion on schwertmannite surface. This contributes to the low adsorption and high desorption capacities of schwertmannite with MREEs and especially with LREEs. However, the distortion is reduced as Lu desorbs at lower pH (e.g., 4.5), becoming reversible without affecting the intrinsic properties of the schwertmannite structure.

None of the non-electrostatic models and EXAFS models conclude whether $LuSO_4^+$ molecules are retained by bidentate or monodentate coordination onto schwertmannite surface. Although both mechanisms can coexist at any pH, as in other Fe-oxyhydroxide minerals (Dardenne et al., 2001), EXAFS models suggest that a decrease in pH enhances the monodentate coordination in the non-desorbed Lu fraction after desorption. Note that the differences in REE coordination onto Fe-oxide phases depend on their crystallinity. Minerals with low crystallinity, such as schwertmannite, could afford some deformation in order to adjust to sorbed molecules in more surface sites (Carrero et al., 2016). Therefore, less constrained sorption sites could allow the coexisting of different sorption coordination.

4.4. Environmental implications

The pH dependence of REE-schwertmannite desorption has widespread environmental implications. An important case is the AMD-impacted estuary of Ría de Huelva (SW Spain), where pH varies

Table 2
Results of the EXAFS fits for LuA sample (sample after Lu adsorption). Model 1: Bidentate binuclear. Model 2: Monodentate mononuclear. Model 3: Monodentate binuclear. The error is expressed in parenthesis after de digit. Var = the number of independent variables.

Model	Neigbor	Path	N	σ2	ΔE0	R	Var	χ2
		Lu-	4	0.0035	8.10	2.38		
1	1st shell	O1	(2)	(2)	(3)	(1)	8	108
		Lu-	4	0.0035	8.10	2.26		
		O2	(2)	(2)	(3)	(4)		
	2nd		2	0.0082	8.10	3.58		
	shell	Lu-S	(2)	(6)	(3)	(1)		
		Lu-		0.0067	8.10	4.52		
		Fe	2fix	(2)	(3)	(5)		
		Lu-	4	0.0035	8.10	2.38		
2	1st shell	O1	(2)	(2)	(3)	(1)	8	111
		Lu-	4	0.0035	8.10	2.26		
		O2	(2)	(2)	(3)	(4)		
	2nd		2	0.0082	8.10	3.58		
	shell	Lu-S	(2)	(6)	(3)	(1)		
		Lu-		0.0059	8.10	4.52		
		Fe	1fix	(3)	(3)	(4)		
		Lu-	4	0.0035	8.10	2.38		
3	1st shell	O1	(2)	(2)	(3)	(1)	9	135
		Lu-	4	0.0035	8.10	2.26		
		O2	(2)	(2)	(3)	(4)		
	2nd		2	0.0082	8.10	3.58		
	shell	Lu-S	(2)	(6)	(3)	(1)		
		Lu-		0.0015	8.10	4.17		
		Fe	2fix	(2)	(3)	(8)		

between 2.5 and 7.5, schwertmannite colloids and sedimentary schwertmannite play a role in the release/retention of oxyanions (e.g., arsenate) and $LnSO_4^+$, and concentrations of REEs change along with the dilution of the AMD by seawater mixture (Elbaz-Poulichet and Dupuy, 1999; Carro et al., 2011; Gutiérrez-León et al., 2024).

Within this context, a sound understanding of REE-schwertmannite sorption/desorption reaction is essential for the fate of toxic REEs in surface waters. REEs retained on schwertmannite colloids at pH above 6.5 would be desorbed if tidal dynamics moves the colloids to areas with lower pH (higher AMD influences). Our study enables us to distinguish three areas in AMD-impacted estuaries as a function of pH. An area with a pH $<$ 4.5 (AMD-river and estuary confluence) where aqueous REE species are not adsorbed by schwertmannite; an area with a pH range of 4.5–6.5 (upstream AMD dilution by seawater mixture) where REE adsorption and desorption occur, and an area with pH $>$ 6.5 (downstream AMD dilution by seawater) where depletion of REEs is caused by REE adsorption on schwertmannite. However, the log DK_{Ln} values calculated in this study differ from the *log* AK_{Ln} values, indicating that desorption is not totally reversible. Thus, REE availability in intermediate areas is lower owing to the surface properties of schwertmannite.

5. Conclusions

REE desorption on schwertmannite is not totally reversible, is pH dependent, and LREEs desorb more strongly than HREEs.

A non-electrostatic model can reproduce the experimental results by implementing the desorption reactions from monodentate and bidentate surface bindings, showing a significant influence of the monodentate desorption reactions at 4.5 $\leq$ pH $<$ 6.5 and bidentate reaction at 6 $\leq$ pH $\leq$ 7. We, therefore, suggest a two-step desorption reaction, where adsorbed bidentate complexes are transformed into monodentate at lower pH and then desorbed.

During desorption, LREEs tend to form monodentate bonding (i.e., n $\approx$ 1.4), whereas bidentate coordination increases with the atomic number (n $\approx$ 1.6 for HREEs). Sc behaves differently as only bidentate surface complexes form. EXAFS is inconclusive for Lu surface coordination but it suggests a bidentate and monodentate coordination under circumneutral pH than seems to convert in monodentate at lower pH.

Differential PDF shows that Lu adsorption results in a structural distortion to accommodate the adsorbed aqueous complex, yielding negative peaks at the Fe—Fe distance from octahedral edge-sharing (R $\approx$ 3.45 Å and $\approx$ 5.45 Å). Considering that Lu is the element of the lanthanide series with the lowest atomic radium, adsorption of LREEs and MREEs would imply a higher structural deformation, accounting too for the high desorption capacity of schwertmannite with MREEs and specially with LREEs. However, the distortion is reduced as Lu desorbs at lower pH (e.g., 4.5), becoming reversible without affecting the intrinsic properties of the schwertmannite structure.

Our results confirm that under AMD conditions (pH $<$ 5) REEs are highly desorbed from schwertmannite. However, under estuarine conditions (pH between 5 and 8), schwertmannite retains the adsorbed REEs in varying degrees. It is probable that the estuary of Huelva is a geochemically favourable system for REE retention by schwertmannite.

The desorption constants obtained in this study are essential to model the geochemical behaviour of REEs under estuarine conditions. Further research on the relationship between schwertmannite surface and other REEs (e.g., Sc that behaves different than lanthanide series) is warranted.

Supplementary data to this article can be found online at https://doi.org/10.1016/j.chemgeo.2024.122588.

CRediT authorship contribution statement

Joan Gutiérrez-León: Writing – original draft, Methodology, Investigation, Formal analysis, Data curation. **Sergio Carrero:** Writing – review & editing, Supervision, Funding acquisition, Data curation, Conceptualization. **Devis Di Tommaso:** Validation, Software, Methodology. **Dimitrios Toroz:** Validation, Software, Methodology. **Alejandro Fernandez-Martinez:** Formal analysis, Conceptualization. **Antonio Aguilar:** Methodology, Formal analysis. **Alba Lozano:** Formal analysis. **Rafael Pérez-López:** Project administration. **Josep M. Soler:** Funding acquisition. **Jordi Cama:** Writing – review & editing, Funding acquisition.

Declaration of competing interest

The authors declare that they have no known competing financial interests or personal relationships that could have appeared to influence the work reported in this paper.

Acknowledgements

This work has been funded by the CGL2017–82331-R, PID2020-119196RB-C21, PID2020-119196RB-C22 and PID2023-153280OA-I00 projects (Spanish Ministry of Economy and Competitiveness), with contribution of FEDER funds, and by the 2021SGR00308 project funded by the Catalan Government. IDAEA-CSIC is a Severo Ochoa Center of Research Excellence (Spanish Ministry of Science and Innovation, Project CEX2018–000794-S). S. Carrero also thanks to Ramon y Cajal Program (RYC2023–04529-I). We would like to acknowledge the technical assistance of N. Moreno, J. Bellés, R. Batrolí and M. Cabañas (IDAEA-CSIC). We also would like to thank the ESRF for beamtime allocation at BM30 and ID22, and their respective reviewing teams (proposals EV-438 and EV-488). We also thank the editor (Dr. Karen H. Johannesson) and three anonymous reviewers for their constructive comments that helped us to improve the quality of the manuscript.

Data availability

Data are available through Mendeley Data at https://doi.org/10.17632/ct3s2xhh5m.1.

References

Acero, P., Ayora, C., Torrentó, C., Nieto, J.M., 2006. The behavior of trace elements during schwertmannite precipitation and subsequent transformation into goethite and jarosite. Geochim. Cosmochim. Acta 70, 4130–4139.

Allen, P.G., Bucher, J.J., Shuh, D.K., Edelstein, N.M., Craig, I., 2000. Coordination chemistry of trivalent lanthanide and actinide ions in dilute and concentrated chloride solutions. Inorg. Chem. 39, 595–601.

Antelo, J., Fiol, S., Gondar, D., López, R., Arce, F., 2012. Comparison of arsenate , chromate and molybdate binding on schwertmannite : Surface adsorption vs anion-exchange. J. Colloid Interface Sci. 386, 338–343.

Ayora, C., Macías, F., Torres, E., Lozano, A., Carrero, S., Nieto, J.M., Pérez-López, R., Fernandez-Martinez, A., Castillo-Michel, H., 2016. Recovery of rare Earth elements and Yttrium from Passive-Remediation Systems of Acid Mine Drainage. Environ. Sci. Technol. 50, 8255–8262.

Ayora, C., Carrero, S., Bellés, J., Basallote, M.D., Cánovas, C.R., Macías, F., 2022. Partition of rare Earth elements between Sulfate Salts formed by the Evaporation of Acid Mine Drainage. Mine Water Environ. 41, 42–57.

Becke, A.D., 1993. Density-functional thermochemistry. III. The role of exact exchange. J. Chem. Phys. 98, 5648–5652.

Bigham, J.M., Nordstrom, D.K., 2000. Iron and aluminum hydroxysulfates from acid sulfate waters. *Sulfate Miner. Crystallogr. Geochemistry*. Environ. Significan. 40, 351–403.

Bigham, J.M., Nordstrom, D.K., 2019. Iron and aluminum hydroxysulfates from acid sulfate waters. In: Sulfate Minerals: Crystallography, Geochemistry, and Environmental Significance Walter de Gruyter GmbH, pp. 351–403.

Bigham, J.M., Schwertmann, U., Carlson, L., Murad, E., 1990. A poorly crystallized oxyhydroxysulfate of iron formed by bacterial oxidation of Fe(II) in acid mine waters. Geochim. Cosmochim. Acta 54, 2743–2758.

Bigham, J.M., Carlson, L., Murad, E., 1994. Schwertmannite, a new iron oxyhydroxysulphate from Pyhäsalmi, Finland, and other localities. Mineral. Mag. 58, 641–648.

Bigham, J.M., Schwertmann, U., Traina, S.J., Winland, R.L., Wolf, M., 1996. Schwertmannite and the chemical modeling of iron in acid sulfate waters. Geochim. Cosmochim. Acta 60, 2111–2121.

Blanc, P., Lassin, A., Piantone, P., Azaroual, M., Jacquemet, N., Fabbri, A., Gaucher, E.C., 2012. Thermoddem: a geochemical database focused on low temperature water/rock interactions and waste materials. Appl. Geochem. 27, 2107–2116.

Burton, E.D., Bush, R.T., Johnston, S.G., Watling, K.M., Hocking, R.K., Sullivan, L.A., Parker, G.K., 2009. Sorption of arsenic(V) and arsenic(III) to schwertmannite. Environ. Sci. Technol. 43, 9202–9207.

Cánovas, C.R., Basallote, M.D., Macías, F., Olías, M., Pérez-López, R., Ayora, C., Nieto, J. M., 2021. Geochemical behaviour and transport of technology critical metals (TCMs) by the Tinto River (SW Spain) to the Atlantic Ocean. Sci. Total Environ. 764, 143796.

Cánovas, C.R., Basallote, M.D., Macías, F., Freydier, R., Parviainen, A., Pérez-López, R., 2022. Thallium distribution in an estuary affected by acid mine drainage (AMD): The Ría de Huelva Estuary (SW Spain). Environ. Pollut. 306.

Carrero, S., Fernandez-Martinez, A., Pérez-López, R., Poulain, A., Salas-Colera, E., Nieto, J.M., 2016. Arsenate and Selenate Scavenging by Basaluminite: Insights into the Reactivity of Aluminum Phases in Acid Mine Drainage.

Carrero, S., Fernandez-Martinez, A., Pérez-López, R., Lee, D., Aquilanti, G., Poulain, A., Lozano, A., Nieto, J.M., 2017. The nanocrystalline structure of basaluminite , an aluminum hydroxide sulfate from acid mine drainage. Am. Mineral. 102, 2381–2389.

Carro, B., Borrego, J., Lopez-Gonzalez, N., Grande, J.A., Gomez, T., de la Torre, M.L., Valente, T., 2011. Impact of acid mine drainage on the hydrogeochemical charcteristics of Tinto-Odiel Estuary (SW Spain). J. od Iber. Geol. 37, 87–96.

Chakhmouradian, A.R., Wall, F., 2012. Rare earth elements: Minerals, mines, magnets (and more). Elements 8, 333–340.

Cossi, M., Rega, N., Scalmani, G., Barone, V., 2003. Energies, structures, and electronic properties of molecules in solution with the C-PCM solvation model. J. Comput. Chem. 24, 669–681.

Dardenne, K., Schäfer, T., Denecke, M.A., Rothe, J., Il, Kim J., 2001. Identification and characterization of sorbed lutetium species on 2-line ferrihydrite by sorption data modeling, TRLFS and EXAFS. Radiochim. Acta 89, 469–479.

Elbaz-Poulichet, F., Dupuy, C., 1999. Behaviour of rare earth elements at the freshwater-seawater interface of two acid mine rivers: the Tinto and Odiel (Andalucia, Spain). Appl. Geochem. 14, 1063–1072.

Ezzat, H., Menazea, A.A., Omara, W., Basyouni, O.H., Helmy, S.A., Mohamed, A.A., Tawfik, W., Ibrahim, M., 2020. Dft: B3lyp/ lanl2dz study for the removal of fe, ni, cu, as, cd and pb with chitosan. Biointerface Res. Appl. Chem. 10, 7002–7010.

Fernandez-Martinez, A., Timon, V., Romaman-Ross, G., Cuello, G.J., Daniels, J.E., Ayora, C., 2010. The structure of schwertmannite, a nanocrystalline iron oxyhydroxysulfate. Am. Mineral. 95, 1312–1322.

Ferreira da Silva, E., Bobos, I., Xavier, Matos J., Patinha, C., Reis, A.P., Cardoso, Fonseca E., 2009. Mineralogy and geochemistry of trace metals and REE in volcanic massive sulfide host rocks, stream sediments, stream waters and acid mine drainage from the Lousal mine area (Iberian Pyrite Belt, Portugal). Appl. Geochem. 24, 383–401.

Finck, N., Bouby, M., Dardenne, K., 2019. Fate of Lu(III) sorbed on 2-line ferrihydrite at pH 5.7 and aged for 12 years at room temperature. I: insights from ICP-OES, XRD, ESEM, AsFlFFF/ICP-MS, and EXAFS spectroscopy. Environ. Sci. Pollut. Res. 26, 5238–5250.

Frisch, M.J., Trucks, G.W., Schlegel, H.B., Scuseria, G.E., Robb, M.A., Cheeseman, J.R., Scalmani, G., Barone, V., Petersson, G.A., Nakatsuji, H., Li, X., Caricato, M., Marenich, A.V., Bloino, J., Janesko, B.G., Gomperts, R., Mennucci, B., Hratchian, H. P., Ortiz, J.V., Izmaylov, A.F., Sonnenberg, J.L., Williams-Young, D., Ding, F., Lipparini, F., Egidi, F., Goings, J., Peng, B., Petrone, A., Henderson, T., Ranasinghe, D., Zakrzewski, V.G., Gao, J., Rega, N., Zheng, G., Liang, W., Hada, M., Ehara, M., Toyota, K., Fukuda, R., Hasegawa, J., Ishida, M., Nakajima, T., Honda, Y., Kitao, O., Nakai, H., Vreven, T., Throssell, K., Montgomery, J.A.J., Peralta, J.E., Ogliaro, F., Bearpark, M.J., Heyd, J.J., Brothers, E.N., Kudin, K.N., Staroverov, V.N., Keith, T.A., Kobayashi, R., Normand, J., Raghavachari, K., Rendell, A.P., Burant, J. C., Iyengar, S.S., Tomasi, J., Cossi, M., Millam, J.M., Klene, M., Adamo, C., Cammi, R., Ochterski, J.W., Martin, R.L., Morokuma, K., Farkas, O., Foresman, J.B., Fox, D.J., 2016. Gaussian 16.

Gutiérrez-León, J., Millán-Becerro, R., Carrero, S., Pérez-López, R., Ceballos, E., Freydier, R., Soler, J.M., Cama, J., 2024. Distribution of trace and rare earth elements in the estuary of Ría de Huelva (SW Spain): Field data and geochemical modeling. Chem. Geol. 662.

Gwenzi, W., Mangori, L., Danha, C., Chaukura, N., Dunjana, N., Sanganyado, E., 2018. Sources, behaviour, and environmental and human health risks of high-technology rare earth elements as emerging contaminants. Sci. Total Environ. 636, 299–313.

Haque, N., Hughes, A., Lim, S., Vernon, C., 2014. Rare earth elements: Overview of mining, mineralogy, uses, sustainability and environmental impact. Resources 3, 614–635.

Hay, P.J., Wadt, W.R., 1985. Ab initio effective core potentials for molecular calculations. Potentials for K to au including the outermost core orbitale. J. Chem. Phys. 82, 299–310.

He, M.L., Wehr, U., Rambeck, W.A., 2010. Effect of low doses of dietary rare earth elements on growth performance of broilers. J. Anim. Physiol. Anim. Nutr. (Berl). 94, 86–92.

Işıldar, A., Rene, E.R., van Hullebusch, E.D., Lens, P.N.L., 2018. Electronic waste as a secondary source of critical metals: Management and recovery technologies. Resour. Conserv. Recycl. 135, 296–312.

Jemmis, E.D., Manoharan, M., Sharma, P.K., 2000. Complexes of C 60 and C 70 : A Theoretical Study. Society, pp. 1879–1887.

Johnson, J., Anderson, C.G., Parkhurst, D.L., 2000. Database thermo.com. V8. R6. 230 Rev. 1.11. Lawrence L.

Jönsson, J., Persson, P., Sjöberg, S., Lövgren, L., 2005. Schwertmannite precipitated from acid mine drainage: phase transformation, sulphate release and surface properties. Appl. Geochem. 20, 179–191.

Juhás, P., Davis, T., Farrow, C.L., Billinge, S.J.L., 2013. PDFgetX3: a rapid and highly automatable program for processing powder diffraction data into total scattering pair distribution functions. J. Appl. Crystallogr. 46, 560–566.

Khamphila, K., Kodama, R., Sato, T., Otake, T., 2017. Adsorption and Post Adsorption Behavior of Schwertmannite with various Oxyanions. J. Miner. Mater. Charact. Eng. 05, 90–106.

Kieffer, J., Karkoulis, D., 2013. PyFAI, a versatile library for azimuthal regrouping. J. Phys. Conf. Ser. 425, 202012.

Klaver, G., Verheul, M., Bakker, I., Petelet-Giraud, E., Négrel, P., 2014. Anthropogenic rare Earth Element in rivers: GADOLINIUM and lanthanum. Partitioning between the dissolved and particulate phases in the Rhine River and spatial propagation through the Rhine-Meuse Delta (the Netherlands). Appl. Geochem. 47, 186–197.

Klungness, G.D., Byrne, R.H., 2000. Comparative hydrolysis behavior of the rare earths and yttrium: the influence of temperature and ionic strength. Polyhedron 19, 99–107.

Kowall, T., Foglia, F., Helm, L., Merbach, A.E., 1995. Molecular dynamics simulation study of lanthanide ions Ln3+ in aqueous solution. Analysis of the structure of the first hydration shell and of the origin of symmetry fluctuations. J. Phys. Chem. 99, 13078–13087.

Lawrence, M.G., Ort, C., Keller, J., 2009. Detection of anthropogenic gadolinium in treated wastewater in South East Queensland. Australia. Water Res. 43, 3534–3540.

Lecomte, K.L., Sarmiento, A.M., Borrego, J., Nieto, J.M., 2017. Rare earth elements mobility processes in an AMD-affected estuary: Huelva Estuary (SW Spain). Mar. Pollut. Bull. 121, 282–291.

Lee, J.H., Byrne, R.H., 1992. Examination of comparative rare earth element complexation behavior using linear free-energy relationships. Geochim. Cosmochim. Acta 56, 1127–1137.

León, R., Macías, F., Cánovas, C.R., Pérez-López, R., Ayora, C., Nieto, J.M., Olías, M., 2021. Mine waters as a secondary source of rare earth elements worldwide: the case of the Iberian Pyrite Belt. J. Geochem. Explor. 224.

Li, J., Hong, M., Yin, X., Liu, J., 2010. Effects of the accumulation of the rare earth elements on soil macrofauna community. J. Rare Earths 28, 957–964.

Li, Y., Mohan, D., Pittman, C.U., Ok, Y.S., Dou, X., 2016. Removal of antimonate and antimonite from water by schwertmannite granules. Desalin. Water Treat. 57, 25639–25652.

Lozano, A., Fernandez-Martinez, A., Ayora, C., Di Tommaso, D., Poulain, A., Rovezzi, M., Marini, C., 2019. Solid and Aqueous Speciation of Yttrium in Passive Remediation Systems of Acid Mine Drainage. Environ. Sci. Technol. 53, 11153–11161.

Lozano, A., Ayora, C., Fernandez-Martinez, A., 2020. Sorption of rare earth elements on schwertmannite and their mobility in acid mine drainage treatments. Appl. Geochem. 113.

Luo, Y.R., Byrne, R.H., 2001. Yttrium and rare Earth element complexation by chloride ions at 25°C. J. Solut. Chem. 30, 837–845.

Luo, Y.R., Byrne, R.H., 2004. Carbonate complexation of yttrium and the rare earth elements in natural waters. Geochim. Cosmochim. Acta 68, 691–699.

Luo, Y., Millero, F.J., 2004. Effects of temperature and ionic strength on the stabilities of the first and second fluoride complexes of yttrium and the rare earth elements. Geochim. Cosmochim. Acta 68, 4301–4308.

Manaka, M., Yanase, N., Sato, T., Fukushi, K., 2007. Natural attenuation of antimony in mine drainage water. Geochem. J. 41, 17–27.

Merten, D., Geletneky, J., Bergmann, H., Haferburg, G., Kothe, E., Büchel, G., 2005. Rare earth element patterns: a tool for understanding processes in remediation of acid mine drainage. Chem. Erde 65, 97–114.
Millero, F.J., 1992. Stability constants for the formation of rare earth-inorganic complexes as a function of ionic strength. Geochim. Cosmochim. Acta 56, 3123–3132.
Moses, C.O., Nordstrom, D.K., Herman, J.S., Mills, A.L., 1987. Aqueous pyrite oxidation by dissolved oxygen and by ferric iron. Geochim. Cosmochim. Acta 51, 1561–1571.
Neira, P., Romero-Freire, A., Basallote, M.D., Qiu, H., Cobelo-García, A., Cánovas, C.R., 2022. Review of the concentration, bioaccumulation, and effects of lanthanides in marine systems. Front. Mar. Sci. 9, 1–14.
Nieto, J.M., Sarmiento, A.M., Canovas, C.R., Olías, M., Ayora, C., 2013. Acid mine drainage in the Iberian Pyrite Belt: 1. Hydrochemical characteristics and pollutant load of the Tinto and Odiel rivers. Environ. Sci. Pollut. Res. 20, 7509–7519.
Noack, C.W., Dzombak, D.A., Karamalidis, A.K., 2014. Rare earth element distributions and trends in natural waters with a focus on groundwater. Environ. Sci. Technol. 48, 4317–4326.
Packman, H., Little, S.H., Nieto, J.M., Basallote, M.D., Pérez-López, R., Coles, B., Kreissig, K., van de Flierdt, T., Rehkämper, M., 2023. Tracing acid mine drainage and estuarine Zn attenuation using Cd and Zn isotopes. Geochim. Cosmochim. Acta 360, 36–56.
Pagano, G., Guida, M., Tommasi, F., Oral, R., 2015. Health effects and toxicity mechanisms of rare earth elements-Knowledge gaps and research prospects. Ecotoxicol. Environ. Saf. 115, 40–48.
Paikaray, S., 2021. Environmental Stability of Schwertmannite: a Review. Mine Water Environ. 40, 570–586.
Paikaray, S., Schröder, C., Peiffer, S., 2017. Schwertmannite stability in anoxic Fe(II)-rich aqueous solution. Geochim. Cosmochim. Acta 217, 292–305.
Parkhurst, D.L., Appelo, C.A.J., 1999. User's guide to PhreeqC (version 2) A computer program for speciation, and inverse geochemical calculations.
Paulick, H., Machacek, E., 2017. The global rare earth element exploration boom: an analysis of resources outside of China and discussion of development perspectives. Res. Policy 52, 134–153.
Pérez-López, R., Millán-Becerro, R., Basallote, M.D., Carrero, S., Parviainen, A., Freydier, R., Macías, F., Cánovas, C.R., 2023. Effects of estuarine water mixing on the mobility of trace elements in acid mine drainage leachates. Mar. Pollut. Bull. 187.
Persson, I., D'Angelo, P., De Panfilis, S., Sandström, M., Eriksson, L., 2008. Hydration of lanthanoid(III) ions in aqueous solution and crystalline hydrates studied by EXAFS spectroscopy and crystallography: The myth of the "gadolinium break". Chem. - A Eur. J. 14, 3056–3066.
Pliego, J.R., Riveros, J.M., 2020. Hybrid discrete-continuum solvation methods. Wiley Interdiscip. Rev. Comput. Mol. Sci. 10, 1–25.
Qin, H.B., Yang, S., Tanaka, M., Sanematsu, K., Arcilla, C., Takahashi, Y., 2021. Scandium immobilization by goethite: Surface adsorption versus structural incorporation. Geochim. Cosmochim. Acta 294, 255–272.
Ravel, B., Newville, M., 2005. ATHENA, ARTEMIS, HEPHAESTUS: data analysis for X-ray absorption spectroscopy using IFEFFIT. J. Synchrotron Radiat. 12, 537–541.
Regenspurg, S., Peiffer, S., 2005. Arsenate and chromate incorporation in schwertmannite. Appl. Geochem. 20, 1226–1239.
Regenspurg, S., Brand, A., Peiffer, S., 2004. Formation and stability of schwertmannite in acidic mining lakes. Geochim. Cosmochim. Acta 68, 1185–1197.
Romero, F.M., Prol-Ledesma, R.M., Canet, C., Alvares, L.N., Pérez-Vázquez, R., 2010. Acid drainage at the inactive Santa Lucia mine, western Cuba: Natural attenuation of arsenic, barium and lead, and geochemical behavior of rare earth elements. Appl. Geochem. 25, 716–727.
Sánchez-España, J., López, Pamo E., Santofimia, E., Aduvire, O., Reyes, J., Barettino, D., 2005. Acid mine drainage in the Iberian Pyrite Belt (Odiel river watershed, Huelva, SW Spain): Geochemistry, mineralogy and environmental implications. Appl. Geochem. 20, 1320–1356.
Schijf, J., Byrne, R.H., 2004. Determination of SO4β1 for yttrium and the rare earth elements at I = 0.66 m and t = 25°C-implications for YREE solution speciation in sulfate-rich waters. Geochim. Cosmochim. Acta 68, 2825–2837.
Schoepfer, V.A., Burton, E.D., 2021. Schwertmannite: A review of its occurrence, formation, structure, stability and interactions with oxyanions. Earth-Science Rev. 221, 103811.
Schoepfer, V.A., Burton, E.D., Johnston, S.G., 2019. Contrasting effects of phosphate on the rapid transformation of schwertmannite to Fe(III) (oxy)hydroxides at near-neutral pH. Geoderma 340, 115–123.
Sestu, M., Navarra, G., Carrero, S., Valvidares, S.M., Aquilanti, G., Pe, R., 2017. Whole-nanoparticle atomistic modeling of the schwertmannite structure from total scattering data research papers. J. Appl. Crystallogr. 50, 1617–1626.
Shi, M., Min, X., Ke, Y., Lin, Z., Yang, Z., Wang, S., Peng, N., Yan, X., Luo, S., Wu, J., Wei, Y., 2021. Recent progress in understanding the mechanism of heavy metals retention by iron (oxyhydr)oxides. Sci. Total Environ. 752, 141930.
Silva, G.C., Bertoli, A.C., Duarte, H.A., Ladeira, A.C.Q., 2022. Recovery of rare earth elements from sulfate-rich acid mine water: looking through the keyhole the exchange reaction for cationic resin. J. Environ. Chem. Eng. 10, 108715.
Spahiu, K., Bruno, J., 1995. A selected thermodynamic database for REE to be used in HLNW performance assessment exercises, p. 88.
Stephen, P.J., Devlin, F.J., Chabalowski, C.F., Frisch, M.J., 1994. Ab Initio Calculation of Vibrational Absorption. J. Phys. Chem. 98, 11623–11627.
Swedlund, P.J., Webster, J.G., 2001. Cu and Zn ternary surface complex formation with so4 on ferrihydrite and schwertmannite. Appl. Geochem. 16, 503–511.
Tan, Q., Li, J., Zeng, X., 2015. Rare Earth elements Recovery from Waste Fluorescent Lamps: a Review. Crit. Rev. Environ. Sci. Technol. 45, 749–776.
Wadt, W.R., Hay, P.J., 1985. Ab initio effective core potentials for molecular calculations. Potentials for main group elements Na to Bi. J. Chem. Phys. 82, 284–298.
Wang, X., Gu, C., Feng, X., Zhu, M., 2015. Sulfate Local Coordination Environment in Schwertmannite. Environ. Sci. Technol. 49, 10440–10448.
Wang, X., Ying, H., Zhao, W., Feng, X., Tan, W., Beyer, K.A., Huang, Q., Liu, F., Zhu, M., 2021. Molecular-Scale Understanding of Sulfate Exchange from Schwertmannite by Chromate Versus Arsenate. Environ. Sci. Technol. 55, 5857–5867.
Webster, J.G., Swedlund, P.J., Webster, K.S., 1998. Trace metal adsorption onto an acid mine drainage iron(III) oxy hydroxy sulfate. Environ. Sci. Technol. 32, 1361–1368.
Weigend, F., Ahlrichs, R., 2005. Balanced basis sets of split valence, triple zeta valence and quadruple zeta valence quality for H to Rn: Design and assessment of accuracy. Phys. Chem. Chem. Phys. 7, 3297–3305.
Wood, S.A., Samson, I.M., 2006. The aqueous geochemistry of gallium, germanium, indium and scandium. Ore Geol. Rev. 28, 57–102.
Yaita, T., Narita, H., Suzuki, S., Tachimori, S., Motohashi, H., Shiwaku, H., 1999. Structural study of lanthanides(III) in aqueous nitrate and chloride solutions by EXAFS. J. Radioanal. Nucl. Chem. 239, 371–375.
Zhang, W., Honaker, R.Q., 2018. Rare earth elements recovery using staged precipitation from a leachate generated from coarse coal refuse. Int. J. Coal Geol. 195, 189–199.
Zhang, S.L., Jia, S.Y., Yu, B., Liu, Y., Wu, S.H., Han, X., 2016. Sulfidization of as(V)-containing schwertmannite and its impact on arsenic mobilization. Chem. Geol. 420, 270–279.
Zhang, D., Zhang, Y., Li, X., Zhang, M., Zou, L., Chi, R., Zhou, F., 2024. The investigation of ion association characteristics in lanthanum sulfate solution by the density functional theory and molecular dynamics simulations. J. Mol. Graph. Model. 127, 108698.